

Direct epitaxial growth of polar (1-x)HfO₂-(x)ZrO₂ ultra-thin films on Silicon

Pavan Nukala^{1,#,*}, Jordi Antoja-Lleonart^{1,#}, Yingfen Wei¹, Lluís Yedra^{2,3}, Brahim Dkhil²,
Beatriz Noheda^{1,*}

1. Zernike Institute of Advanced Materials, University of Groningen, 9747 AG, The Netherlands
2. Laboratoire Structures, Propriétés et Modélisation des Solides, CentraleSupélec, CNRS-UMR8580, Université Paris-Saclay, 91190 Gif-sur-Yvette, France
3. Laboratoire Mécanique des Sols, Structures et Matériaux, CentraleSupélec, CNRS UMR 8579, Université Paris-Saclay, 91190 Gif-sur-Yvette, France

equally contributing authors

*Corresponding authors, email: p.nukala@rug.nl, b.noheda@rug.nl

Abstract: Ultra-thin Hf_{1-x}Zr_xO₂ films have attracted tremendous interest owing to their Si-compatible ferroelectricity arising from polar polymorphs. While these phases have been grown on Si as polycrystalline films, epitaxial growth was only achieved on non-Si substrates. Here we report direct epitaxy of polar phases on Si using pulsed laser deposition enabled via *in situ* scavenging of the native a-SiO_x under ballistic conditions. On Si (111), polar rhombohedral (r)-phase and bulk monoclinic (m-) phase coexist, with the volume of the former increasing with increasing Zr concentration. R-phase is stabilized in the regions with a direct connection between the substrate and the film through the compressive strain provided by an interfacial crystalline c-SiO₂ layer., The film relaxes to a bulk m-phase in regions where a-SiO_x regrows. On Si (100), we observe polar orthorhombic o-phase coexisting with m-phase, stabilized by inhomogeneous strains at the intersection of monoclinic domains. This work provides fundamental insight into the conditions that lead to the preferential stabilization of r-, o- and m-phases.

Introduction:

Ferroelectric hafnia-based thin-films¹ have by now been established as the most promising materials to realize the potential of ferroelectric phenomena in real devices^{2,3}. Their Si compatibility, simple chemistry and unique ferroelectricity, that becomes more robust with miniaturization, is tailor-made for microelectronics, offering ready-made alternatives to conventional ferroelectrics that lack all these attributes⁴⁻¹². Such distinguishing characteristics

lead to an upsurge in application-oriented research as well as in curiosity-driven fundamental research to solve questions such as why these materials are capable of sustaining the unconventional ferroelectricity^{13–32}, how these materials negate the effects of depolarization fields^{33,34}, and whether such a new type of ferroelectricity can be replicated in other simple oxide systems.

A prominent feature of hafnia-based materials is polymorphism³⁵. While the ground state in the bulk HfO₂ is a non-polar monoclinic (m-, *P2₁/c*) phase, a plethora of low-volume both polar and non-polar metastable states can be stabilized at ambient conditions via a combination of strategies such as cationic and anionic doping^{1,25–27,29,32}, thermal and inhomogeneous stresses^{36,37}, nanostructuring³⁸, epitaxial strain^{16,20,22,23,26,29,39–42}, and oxygen vacancy engineering^{43,44}, all of which can be suitably engineered into thin-film geometries. Based on first-principles calculations^{15,39,45–47} at least five polar polymorphs (with space groups *Pca2₁*, *Cc*, *Pmn2₁*, *R3* and *R3m*) can be identified as those that can be experimentally obtained. Owing to its relatively low energy, the orthorhombic (o-) *Pca2₁* phase is widely observed in hafnia-based films grown via atomic layer deposition (ALD)^{1,17,24,25}, chemical solution deposition (CSD)²⁸, RF sputtering on Si^{18,21} and pulsed-laser deposition (PLD) on selected substrates^{19,23,26,31,40–42}. A slightly higher energy rhombohedral (r-) phase (*R3m* or *R3*) has been recently observed on epitaxial Hf_{1/2}Zr_{1/2}O₂ films grown on SrTiO₃ (STO)³⁹. The r-phase is stabilized by a combination of the large surface energy induced internal pressure of the nanoparticles and the substrate-imposed compressive strain. The epitaxial growth of the r-phase enabled the observation of the highest values of spontaneous polarization ($P_s = 34 \mu\text{C}/\text{cm}^2$) in HfO₂-ZrO₂ systems, although they showed larger coercive fields than films in the polar o-phase.

So far, polar phases have been successfully obtained via epitaxial synthesis techniques (PLD) on a variety of substrates: perovskites^{16,40–42} (including buffered STO on Si (001))⁴², fluorites^{19,23,26} and hexagonal substrates⁴⁸. However, the advantages gained by epitaxy are offset by the fact that none of these films are grown directly on Si, despite the Si integrability of hafnia-based systems. It is in this context that we explore for the first time the epitaxy of polar polymorphs in (1-x)HfO₂-xZrO₂ (HZO (x)) films directly on Si.

Direct epitaxial growth of oxides on Si is complicated by the presence of a very thin amorphous native oxide layer, which prevents the transfer of texture from the substrate to the film. This interfacial layer can be removed prior to deposition through hydrofluoric (acid etching), which lowers the crystalline quality^{49,50}. However, the epitaxial growth of yttria-stabilized zirconia (YSZ) on Si (100) is a mature process^{51–54}, as witnessed by the fact that YSZ-

buffered Si (100) substrates are commonly used for the growth of high- T_c superconductors and other functional layers⁵⁵⁻⁵⁹. The problem of native oxide in YSZ on Si is solved via an *in situ* scavenging process through Zr (Y), because the formation energy of ZrO_2 (Y_2O_3) is less than that of SiO_2 .^{50,57,60}. In other words, one (or both) of the following decomposition chemical reactions takes place during the initial stages of YSZ growth enabling a transfer of substrate texture.



The rest of the YSZ growth follows the template set by the crystalline ZrO_2 seed, formed as a result of scavenging the native amorphous oxide, resulting in a very high crystalline quality. Strain relaxation of thicker layers of YSZ happens *via* the regrowth of the a- SiO_2 oxide (backward reactions 1 and 2, upon increasing the amount of product), and through other standard epitaxial relaxation processes such as generation of misfit dislocations. Inspired by the success of direct epitaxy of a sister compound YSZ on Si, here we report successful growth of epitaxial polar phases of HfO_2 - ZrO_2 alloys directly on Si (111) and Si (100).

Experimental Methods:

PLD was used for the deposition of HZO (x) with x=0.5, 0.7 and 0.85 on *p*-doped Si (111) (resistivity < 0.005 Ω cm), and Si (100) (resistivity < 0.03 Ω cm). Targets of the desired compositions (x=0.5, 0.7, 0.85) were prepared through standard solid-state synthesis starting from powders of HfO_2 (99% purity) and ZrO_2 (99.5 % purity). A KrF excimer laser ($\lambda=248$ nm) was used for target ablation at a fluence of 1.1 J cm^{-2} . A base pressure of 10^{-7} torr was maintained in the deposition chamber. Target to substrate distance was fixed at 50 mm. HZO layers were deposited at 800°C with the flow of Ar carrier gas (5 sccm) at a process pressure of 0.005 mbar and laser repetition rate of 7 Hz.

The choice of target-substrate distance, as well as the low pressure conditions, ensured a ballistic mode of deposition, preventing the oxidation of atomic species (Hf, Zr ions) in the plasma itself. It is indeed crucial for the interfacial scavenging reactions that species transported to the substrate are Hf, Zr and O ions with no ionized HfO_2 and ZrO_2 present in the plasma. The 7 Hz repetition rate favors nucleation-dominated kinetics, or in this case, the occurrence of interfacial scavenging at multiple locations, and thus the generation of several (Hf) ZrO_2 seeds or growth templates.

On Si(111), HZO (x) films of 10 nm thickness with three different compositions (x=0.5, 0.7, 0.85) were deposited, at a growth rate of 0.7 Å/sec. On Si(100), films of 5, 10 and 20 nm were deposited with composition x=0.7, at a growth rate of 0.9 Å/sec. Thickness was confirmed from both Scanning Transmission Electron Microscopy (STEM) and x-ray reflectivity measurements. Information about global structure, symmetry, phase-mixing and domains was inferred from x-ray diffraction (XRD) with a Cu K α source. Texture analysis was performed *via* χ - ϕ (pole figure) scans at $2\theta \approx 30.0^\circ$ (approximately corresponding to the $d_{\{111\}}$ of the low-volume phases) and at $2\theta \approx 34.5^\circ$ (approximately corresponding to the $d_{\{200\}}$ of all the polymorphs). The d-spacings of the poles obtained from the χ - ϕ stereographic projections were more precisely analysed through θ - 2θ scans around them, which from here on will be referred to as ‘pole-slicing’.

Local structural characterization and phase analysis was performed through STEM imaging at 200 kV (Titan G2 and Themis). STEM images were obtained in both high-angle annular dark field (HAADF) mode, and bright-field (BF) mode. Chemical maps were generated via energy dispersive spectroscopy (EDS) in a four detector ChemiSTEM set-up on the Titan G2 aberration-corrected electron microscope.

Results and discussion:

(1-x)HfO₂- xZrO₂ on Si (111)

Strongly textured (111) films: Pole figures obtained from films with x=0.5 (Fig. 1a), 0.7 and 0.85 (*Supplementary Fig. S1a*) about $2\theta = 30.0^\circ$ look qualitatively similar. In addition to the peak at the center (out-of-plane), there are three poles (P1 to P3) arising from the film at $\chi \sim 71^\circ$ separated from each other in ϕ by $\sim 120^\circ$. The weaker poles at $\chi \sim 71^\circ$ (Fig. 1a) are from the tail of the substrate peak at $2\theta = 28.44^\circ$. This symmetry is consistent with $\langle 111 \rangle$ -oriented films, following the substrate. Quite interestingly, the $\{111\}$ poles corresponding to the substrate and the film are rotated 180° about the substrate normal.

Phase coexistence and evidence of r-phase: On the films with x=0.5, the pole slicing across P1 to P3 clearly shows two peaks at every pole centered with $2\theta = 28.5^\circ$ and 31.4° (Fig. 1b), corresponding to $d_{\{111\}}$ and $d_{\{11\bar{1}\}}$ of the bulk m-phase. With the increase of Zr concentration to x=0.7 (arrow in Fig. 1c), a peak corresponding to a low-volume phase starts to appear at $2\theta = 30.23^\circ$, with the majority phase still being monoclinic. A further increase in Zr concentration changes the predominant phase of the film to this low volume phase, with very minor fraction in the m-phase (Fig. 1d). To determine the symmetry of the low-volume phase

for the films with $x=0.85$, a three peak Gaussian fitting was performed to the pole-slicing plots from P1, P2 and P3 between 2θ of 27° and 33° , (*Supplementary Fig. S1b*). The peak position representing the low-volume phase is at $2\theta=30.24\pm 0.03^\circ$ for P1, P2 and P3 whereas the out-of-plane peak is at $2\theta=30.12\pm 0.04^\circ$ (see Fig. 2a-b, as well as *supplementary information*, Fig. S2, for error estimation from pole-slicing that can occur through slight misalignment and inhomogeneous strain). Such a 3:1 multiplicity in $d_{\{111\}}$ is consistent with the low-volume phase having a rhombohedral symmetry, a phase which was recently discovered on films grown epitaxially on STO substrates³⁹. The $d_{\{111\}}$ and $d_{\{11-1\}}$ can be calculated to be $2.96 (\pm 0.01) \text{ \AA}$ and $2.95 (\pm 0.01) \text{ \AA}$, respectively, and this corresponds to a unit cell with $a=b=c\approx 5.11 (\pm 0.01) \text{ \AA}$ and rhombohedral angle (α) between 89.9° and 90° . This distortion is smaller than what was observed on the 10 nm HZO ($x=0.5$) films grown on STO ($\alpha\sim 89.3^\circ$)³⁹. Pole figures of the $\{002\}$ planes obtained around $2\theta=35^\circ$ and corresponding pole-slicing further confirm these lattice parameters (*Supplementary Fig. S3*).

HAADF-STEM images acquired on cross-sectional samples of films with $x=0.5$ clearly show that the entire film is in the monoclinic (non-polar) phase, consistent with the XRD data. EDS analysis shows a contiguous layer of amorphous $a\text{-SiO}_x$ of ~ 0.5 to 1 nm between Si and the HZO layer (*Supplementary Fig. S4*). This is a reformed oxide layer, a result of the backward reaction upon increasing the product concentration in the scavenging chemical reactions 1 and 2. With Zr concentration increased to $x=0.7$, this $a\text{-SiO}_x$ layer exists in some regions, but is absent in some other regions (Fig. 2c), a clear testimony to the better scavenging properties of Zr ions compared to Hf ions. Very interestingly, upon analyzing the $d_{\{111\}}$ lattice parameters, we find that the film just above the regions with the $a\text{-SiO}_x$ layer displays a monoclinic non-polar phase ($d_{\{11-1\}}\approx 2.82 \text{ \AA}$, $d_{\{111\}}\approx 3.13 \text{ \AA}$), while the film directly in contact with Si substrate is in the low volume phase (Fig. 2c, zoomed in Fig. 2d). HAADF-STEM multislice image (200 KV) simulations (Fig. 2e) obtained from the rhombohedral ($R3$) phase (cross-sectional sample thickness of ~ 20 nm), among all the other polymorphs, show the closest resemblance to our images. In particular, the alternating intensity of the cationic columns along the $\langle 112 \rangle$ direction is a distinct feature of the rhombohedral polar phases (both $R3$ and $R3m$), which can be seen in our experimental images (Fig. 2d and 2f).

Interfacial phase, and epitaxy: At the interface between Si and r-phase HZO, we observe at least two monolayers of crystalline phase, which is different from both the Si and HZO structures, as shown in the bright field STEM image in Fig. 3a (contrast digitally inverted). This is most likely a crystalline, tridymite or β -cristobalite, phase of SiO_2 , which has been

studied in detail at the Si/a-SiO_x interfaces, and is well-known to induce epitaxy between Si and YSZ layers^{50,61–63}. In Fig. 3b, we propose a rough schematic for epitaxy, based on Fig. 3a, assuming the lattice parameters of the β -cristobalite as the crystalline c-SiO₂ phase (in-plane $\sim 3.55 \text{ \AA}$). Epitaxy of HZO (in-plane $\sim 3.6 \text{ \AA}$) on c-SiO₂ thus provides initial compressive strain boundary conditions.

These results enable us to propose that the phase of the initial seed formed as a result of scavenging the native oxide is the low-volume r-phase. The compressive strain conditions stabilize the r-phase, quite similar to HZO films grown on STO³⁹. However, regrowth of amorphous oxide layer relaxes the strain, stabilizing the non-polar m-phase⁵⁰. Increasing the Zr content increases the efficiency of the native oxide scavenging, thus stabilizing a greater volume of the film in the r-phase.

Polar nature of the r-phase: Metal-insulator-semiconductor (MIS) capacitors were fabricated on these films with TiN (200 μm diameter) as the top-electrode. These were quite leaky especially in the inversion regime of operation. Cooling the devices to 10 K reduced the leakage, despite not completely avoiding it. On the films with $x=0.7$, very weak polarization switching (evident from I-V loop) was observed with ΔP_s of $\sim 2 \mu\text{C}/\text{cm}^2$ (Fig. 3c), with devices tested at 1000 Hz. While the device optimization and rigorous electrical characterization is a subject of future work, these measurements demonstrate that the r-phase is indeed polar. About the weak ferroelectric switching, apart from the fact that these samples show a predominant fraction of non-polar m-phase, it must also be noted that the rhombohedral angle in our samples is very close to 90° . First-principles calculations³⁹ show that at these low distortions, the phase with $R3m$ symmetry has very low $P_s \sim 1 \mu\text{C}/\text{cm}^2$.

(0.3) HfO₂- (0.7)ZrO₂ on Si (100)

Textured {100} films, and thickness dependence: On 5 nm thick films (Fig. 4a-b), pole figures about $2\theta=31^\circ$ (approximately $d_{\{111\}}$ of HZO) show 4 {111} poles at $\chi \approx 53^\circ$ separated in ϕ by 90° (Fig. 4a). Combined with the pole figure data at $2\theta=34^\circ$, which shows a {200}-pole at $\chi \approx 0^\circ$ (Fig. 4b), it is evident that these films are strongly textured with {100} planes parallel to the Si (100) surface. On 10 nm thick films (Fig. 4c,d), along with all the poles observed for the 5 nm films, some extra satellites appear. Specifically, two satellites appear at $\chi \approx 58^\circ$ for every intense {111} pole (at $\chi \approx 53^\circ$) separated in ϕ by $\sim 7^\circ$ (Fig. 4c). About the intense center {100} pole, 4 different satellites appear centered at $\chi \approx 8^\circ$ (with a spread of $8\text{-}10^\circ$) separated in ϕ by 90° (Fig. 4d). These satellites hint of domains/grains where the {100} planes

are misoriented with respect to Si (100) surface. As the thickness of the film increases to 20 nm (Fig. 4e,f), poles from these misoriented grains become the most intense and the signal from the domains with $\{100\} // \text{Si (100)}$ domains almost disappears.

Phase coexistence, domains and accordions: To further learn about the lattice parameters and global symmetries, pole-slicing was performed across each of these pole figures. Here we discuss the results from 10 nm films on Si (100), which include all the features of both the 5 nm and the 20 nm films. Around the $\{111\}$ pole (zoomed in view in Fig. 5a), when aligned perfectly either at $\chi \approx 53^\circ$ (pixel 1 (black) in Fig. 5a), or at the most intense spot of the satellites ($\chi \approx 58^\circ$, grey pixels 10 and 11 in Fig. 5a), pole-slicing clearly shows two distinct peaks centered at $2\theta = 28.5^\circ$ and 31.5° (Fig. 5b). This is a signature of the monoclinic phase, and its corresponding domain structure. In particular, the monoclinic domains that give rise to these Bragg peaks (at χ and ϕ of the pixels 1, 10 and 11 in Fig. 5b), correspond to two types of domains: those having the a-b plane // Si(001) (dominating in thinner samples), and those with the a-b plane a few degrees misoriented from Si (001) (in thicker samples), as sketched in Fig. 5c. The separation in ϕ of the satellites is a result of domains with positive and negative misorientation. Rigorous proof of this model through a complete mathematical analysis of the pole figure analysis is provided in the supplementary information (*Supplementary Fig. S5, 6* and related text).

When pole slicing is performed at χ values in between the black and grey pixels (purposely “misaligned”) in Fig. 5a (pixels 4,5 (red) and 3,4 (orange) pixels), we find the emergence of a third peak at $2\theta \approx 30.2^\circ$ in addition to the two monoclinic $\{111\}$ peaks (Fig. 5b). This corresponds to a low-volume minor phase that coexists with the major bulk-monoclinic phase.

Overview cross-sectional HAADF-STEM image acquired along the $[010]$ zone (Fig. 6a) on the 10 nm thick film clearly shows an accordion-like domain morphology. Upon further zooming in (blue box in Fig. 6a), we see the domains that contribute to the zig-zag pattern correspond very well to the monoclinic symmetry (HAADF-STEM simulation in Fig. 6b). The monoclinic angle (β) varies between 81° and 85° across various domains. This variation is indeed reflected as the spread of the satellite spots about $\chi = 8^\circ$ in the $\{001\}$ pole figure (Fig. 4d). Intersection of two domains with positive and negative misorientation (9 and -9° in Fig. 6b) of the ab plane with Si (001), results in the accordion morphology, consistent with the satellite spots of the $\{111\}$ poles in XRD analysis. The monoclinic domains corresponding to ab plane // Si (001) are shown in the supplementary information (*Supplementary Fig. S7*).

The region enclosed in red in Fig. 6a, when zoomed and further analysed is consistent with our HAADF-STEM simulations from an orthorhombic crystal (Fig. 6c), and not the other low-volume polymorphs (simulations of various polymorphs are compared in *Supplementary Fig.S8*). Interplanar (d) spacings for various crystallographic planes obtained from the HAADF-STEM image Fourier transform (Fig. 6c), match very well with o-phase bulk lattice parameters⁶⁴. In particular, $d_{(\text{in-plane})}=2.51\pm 0.02 \text{ \AA}$, and $d_{(\text{out-of-plane})}=2.57\pm 0.02 \text{ \AA}$, correspond to $d_{(002)}$ and $d_{(200)}$ for the o-phase, suggesting that the polar axis (*c*-axis in *Pca2₁* symmetry) is in-plane. Thus STEM analysis conclusively shows that, in addition to the various kinds of monoclinic domains (Fig. 5c), a low-volume o-phase, the commonly occurring low-energy ferroelectric phase in polycrystalline thin films, is also present in these films.

Interface and epitaxy: From EDS chemical maps (Fig. 7a) and Wiener filtered HAADF-STEM images (Fig. 7b) at the interface between HZO and Si (100), it is quite clear that a contiguous layer of <1 nm regrown a-SiO_x exists. Furthermore, there also seems to be an interface c-SiO₂ (β -cristobalite, most likely) structure between Si(100) and the a-SiO_x, which enables epitaxy on Si(001)^{50,61-63}. The in-plane lattice parameter of β -cristobalite (5.03 \AA) imposes a compressive strain on any polymorph of HZO. However, the regrowth of a-SiO_x relaxes this strain stabilizing most of the film in a bulk m-phase. Notably, the grains stabilizing in the o-phase also are interfaced with regrown a-SiO_x. This is unlike growth of HZO ($x=0.7$) on Si (111), where there is a clear correlation between the existence of a low-volume phase, and the absence of regrown a-SiO_x on Si. Thus, it appears that the stabilization of o-phase is a result of the inhomogeneous strain fields originating at the intersection of various kinds of nanoscopic monoclinic domains that form the accordion, and not because of strain transfer from the substrate.

Polar r-phase vs. polar o-phase

Among all the polar polymorphs of hafnia, first principles calculations suggest that the o-phase (*Pca2₁*) has the least energy (64 meV f.u.⁻¹ with respect to the ground state)³⁹. The rhombohedral polymorphs (*R3m*: 158 meV f.u.⁻¹ and *R3*: 195 meV f.u.⁻¹), though more energetic, seem more favorable to obtain experimentally, under a combination of compressive strain and quite notably a (111) film orientation. Both the films grown on STO substrates by Wei et al.,³⁹ and the films grown on Si(111) in the current work satisfy these conditions, and thus exhibit a polar r-phase (and not the low-energy o-phase). These observations, however, are quite contradictory to the theoretical predictions of Liu and Hanrahan²², possibly owing to the absence of the r-phases in their calculations. It must also be noted that films grown in (001)

orientation in this work, show a preference for the o-phase, and not the r-phase. Such an orientation dependence of the obtained polar phase is very unique, and deserves further investigation.

Conclusions:

(1-x)HfO₂-(x)ZrO₂ (HZO) with various compositions in the range 0.5 < x < 0.85 were grown epitaxially on Si(111) and Si(100), without using buffer layers, using PLD. *In situ* scavenging of the native oxide using decomposition reactions plays a crucial role in achieving epitaxy directly on Si. On both these substrates, an interfacial phase of c-SiO₂ (most likely β -cristobalite) has been found, and it offers initial compressive strain conditions for the growth of HZO. The regrowth of an amorphous a-SiO_x interlayer is a relaxation mechanism to release strain. On Si (111), the film on the top of the regions of regrown amorphous oxide relaxes to a bulk non-polar monoclinic phase, and the film directly in connection with the c-SiO₂ is in the polar r-phase. The volume fraction of the r-phase increases and the regrown a-SiO_x decreases with increasing Zr content, owing to better reactivity of Zr to participate in the a-SiO_x scavenging reaction (compared to Hf). Ferroelectric measurements show leaky and incipient, but clear, P-E hysteresis loops, an evidence to the polar nature of the r-phase. On Si (100), the observed polar o-phase seems to be stabilized by inhomogeneous strains arising out of nanodomain coexistence of the surrounding m-phase. Finally, in addition to strain and surface energy, there also appears to be an orientational dependence to the stabilization of polar phases (at least on Si), i.e. the r-phase is favored in (111) orientation, while the o-phase is preferred in (001).

Acknowledgements: PN acknowledges the funding received from European Union's Horizon 2020 research and innovation programme under Marie Skłodowska-Curie grant agreement No: 794954 (Project name: FERHAZ). JA and BN acknowledge the funding from NWO's TOP-PUNT grant 718.016002. YW and BN acknowledge the China Scholarship Council. LY and BD acknowledge a public grant overseen by the French National Research Agency (ANR) as a part of the 'Investissements d'Avenir' program (grant no. ANR-10-EQPX-37, EquipEx MATMECA) and through ANR-17-CE24-0032/EXPAND.

References:

1. Schroeder, U., Hwang, C., Funakubo, H. *Ferroelectricity in doped hafnium oxide*. (1st

- edition, Woodhead Publishing 2019).
2. Böske, T. S., Müller, J., Bräuhaus, D., Schröder, U. & Böttger, U. Ferroelectricity in hafnium oxide thin films. *Appl. Phys. Lett.* **99**, 102903 (2011).
 3. Park, M. H., Lee, Y. H., Mikolajick, T., Schroeder, U. & Hwang, C. S. Review and perspective on ferroelectric HfO₂-based thin films for memory applications. **8**, 795, *MRS Commun.* (2018).
 4. Polakowski, P. *et al.* Ferroelectric deep trench capacitors based on Al:HfO₂ for 3D nonvolatile memory applications. in *2014 IEEE 6th International Memory Workshop, IMW 2014* (2014).
 5. Pešić, M., Hoffmann, M., Richter, C., Mikolajick, T. & Schroeder, U. Nonvolatile Random Access Memory and Energy Storage Based on Antiferroelectric Like Hysteresis in ZrO₂. *Adv. Funct. Mater.* **26**, 7486 (2016).
 6. Mulaosmanovic, H. *et al.* Novel ferroelectric FET based synapse for neuromorphic systems. in *Digest of Technical Papers - Symposium on VLSI Technology* (2017).
 7. Müller, J. *et al.* Ferroelectricity in HfO₂ enables nonvolatile data storage in 28 nm HKMG. in *Digest of Technical Papers - Symposium on VLSI Technology* (2012).
 8. Muller, J. *et al.* Ferroelectric hafnium oxide: A CMOS-compatible and highly scalable approach to future ferroelectric memories. in *Technical Digest - International Electron Devices Meeting, IEDM* (2013).
 9. Wei, Y. *et al.* Magnetic tunnel junctions based on ferroelectric Hf_{0.5}Zr_{0.5}O₂ tunnel barriers. *arXiv:1902.08021* (2019).
 10. Fan, C. C. *et al.* Achieving high-scalability negative capacitance FETs with uniform Sub-35 mV/dec switch using dopant-free hafnium oxide and gate strain. in *Digest of Technical Papers - Symposium on VLSI Technology* (2018).
 11. Dragoman, M. *et al.* Very large phase shift of microwave signals in a 6 nm Hf_xZr_{1-x}O₂ ferroelectric at ±3 V. *Nanotechnology* **28**, 38LT04 (2017).
 12. Müller, J. *et al.* Ferroelectric Zr_{0.5}Hf_{0.5}O₂ thin films for nonvolatile memory applications. *Appl. Phys. Lett.* **99**, 112901 (2011).
 13. Park, M. H. *et al.* Morphotropic Phase Boundary of Hf_{1-x}Zr_xO₂ Thin Films for Dynamic

- Random Access Memories. *ACS Appl. Mater. Interfaces*, **10**, 42666 (2018).
14. Sang, X., Grimley, E. D., Schenk, T., Schroeder, U. & Lebeau, J. M. On the structural origins of ferroelectricity in HfO₂ thin films. *Appl. Phys. Lett.* **106**, 162905 (2015).
 15. Barabash, S. V. Prediction of new metastable HfO₂ phases: toward understanding ferro- and antiferroelectric films. *J. Comput. Electron.* **16**, 1227 (2017).
 16. Lyu, J., Fina, I., Solanas, R., Fontcuberta, J. & Sánchez, F. Growth Window of Ferroelectric Epitaxial Hf_{0.5}Zr_{0.5}O₂ Thin Films. *ACS Appl. Electron. Mater.* **1**, 220–228 (2019).
 17. Zacharaki, C. *et al.* Very large remanent polarization in ferroelectric Hf_{1-x}Zr_xO₂ grown on Ge substrates by plasma assisted atomic oxygen deposition. *Appl. Phys. Lett.* **114**, 112901, (2019).
 18. Luo, Q. *et al.* Composition-Dependent Ferroelectric Properties in Sputtered Hf_xZr_{1-x}O₂ Thin Films. *IEEE Electron Device Lett.* **40**, 570–573 (2019).
 19. Katayama, K. *et al.* Orientation control and domain structure analysis of {100}-oriented epitaxial ferroelectric orthorhombic HfO₂-based thin films. *J. Appl. Phys.* **119**, 134101 (2016).
 20. Park, M. H., Kim, H. J., Kim, Y. J., Moon, T. & Hwang, C. S. The effects of crystallographic orientation and strain of thin Hf_{0.5}Zr_{0.5}O₂ film on its ferroelectricity. *Appl. Phys. Lett.* **104**, 072901 (2014).
 21. Bouaziz, J., Romeo, P. R., Baboux, N. & Vilquin, B. Characterization of ferroelectric hafnium/zirconium oxide solid solutions deposited by reactive magnetron sputtering. *J. Vac. Sci. Technol. B* **37**, 021203 (2019).
 22. Liu, S. & Hanrahan, B. M. Effects of growth orientations and epitaxial strains on phase stability of HfO₂ thin films. *Phys. Rev. Mater.* **3**, 054404 (2019).
 23. Shimizu, T. *et al.* The demonstration of significant ferroelectricity in epitaxial Y-doped HfO₂ film. *Sci. Rep.* 32931 (2016).
 24. Müller, J. *et al.* Ferroelectricity in Simple Binary ZrO₂ and HfO₂. *Nano Lett* **12**, 4318 (2012).
 25. Florent, K. *et al.* Understanding ferroelectric Al:HfO₂ thin films with Si-based electrodes

- for 3D applications. *J. Appl. Phys.* **121**, 204103 (2017).
26. Shimizu, T. *et al.* Growth of epitaxial orthorhombic $\text{YO}_{1.5}$ -substituted HfO_2 thin film. *Appl. Phys. Lett.* **107**, 032910 (2015).
 27. Schroeder, U. *et al.* Impact of different dopants on the switching properties of ferroelectric hafnium oxide. *Japanese Journal of Applied Physics* **53**, 08LE02 (2014).
 28. Starschich, S., Griesche, D., Schneller, T. & Böttger, U. Chemical Solution Deposition of Ferroelectric Hafnium Oxide for Future Lead Free Ferroelectric Devices. *ECS J. Solid State Sci. Technol.* **4**, P419 (2015).
 29. Sharma, Y., Barrionuevo, D., Agarwal, R., Pavunny, S. P. & Katiyar, R. S. Ferroelectricity in Rare-Earth Modified Hafnia Thin Films Deposited by Sequential Pulsed Laser Deposition. *ECS Solid State Lett.* **4**, N13 (2015).
 30. Grimley, E. D. *et al.* Structural Changes Underlying Field-Cycling Phenomena in Ferroelectric HfO_2 Thin Films. *Adv. Electron. Mater.* **2**, 1600173 (2016).
 31. Lyu, J., Fina, I., Solanas, R., Fontcuberta, J. & Sánchez, F. Robust ferroelectricity in epitaxial $\text{Hf}_{1/2}\text{Zr}_{1/2}\text{O}_2$ thin films. *Appl. Phys. Lett.* **113**, 082902 (2018).
 32. Hoffmann, M. *et al.* Stabilizing the ferroelectric phase in doped hafnium oxide. *J. Appl. Phys.* **118**, 072006 (2015).
 33. Schenk, T. *et al.* Complex internal bias fields in ferroelectric hafnium oxide. *ACS Appl. Mater. Interfaces* **7**, 20224 (2015).
 34. Chouprik, A. *et al.* Ferroelectricity in $\text{Hf}_{0.5}\text{Zr}_{0.5}\text{O}_2$ Thin Films: A Microscopic Study of the Polarization Switching Phenomenon and Field-Induced Phase Transformations. *ACS Appl. Mater. Interfaces* **10**, 8818 (2018).
 35. Li, P., Chen, I. W. & Penner-Hahn, J. E. X-ray-absorption studies of zirconia polymorphs. I. Characteristic local structures. *Phys. Rev. B* **48**, 10063 (1993).
 36. Howard, C. J., Kisi, E. H., Roberts, R. B. & Hill, R. J. Neutron Diffraction Studies of Phase Transformations between Tetragonal and Orthorhombic Zirconia in Magnesia-Partially-Stabilized Zirconia. *J. Am. Ceram. Soc.* **73**, 2828 (1990).
 37. Adams, D. M., Leonard, S., Russell, D. R. & Cernik, R. J. X-ray diffraction study of Hafnia under high pressure using synchrotron radiation. *J. Phys. Chem. Solids* **52**, 1181

- (1991).
38. Sharma, G., Ushakov, S. V. & Navrotsky, A. Size driven thermodynamic crossovers in phase stability in zirconia and hafnia. *J. Am. Ceram. Soc.* **101**, 31 (2018).
 39. Wei, Y. *et al.* A rhombohedral ferroelectric phase in epitaxially strained Hf_{0.5}Zr_{0.5}O₂ thin films. *Nat. Mater.* **17**, 1095 (2018).
 40. Lyu, J. *et al.* Enhanced ferroelectricity in epitaxial Hf_{0.5}Zr_{0.5}O₂ thin films integrated with Si(001) using SrTiO₃ templates. *Appl. Phys. Lett.* **114**, 222901 (2019).
 41. Yoong, H. Y. *et al.* Epitaxial Ferroelectric Hf_{0.5}Zr_{0.5}O₂ Thin Films and Their Implementations in Memristors for Brain-Inspired Computing. *Adv. Funct. Mater.* **50**, 1806037 (2018).
 42. Lyu, J., Fina, I., Fontcuberta, J. & Sánchez, F. Epitaxial Integration on Si(001) of Ferroelectric Hf_{0.5}Zr_{0.5}O₂ Capacitors with High Retention and Endurance. *ACS Appl. Mater. Interfaces* **11**, 6224 (2019).
 43. Moya, J. S., Moreno, R., Requena, J. & Soria, J. Black Color in Partially Stabilized Zirconia. *J. Am. Ceram. Soc.* **74**, 1745 (1988).
 44. Sharath, S. U. *et al.* Control of Switching Modes and Conductance Quantization in Oxygen Engineered HfO_x based Memristive Devices. *Adv. Funct. Mater.* **27**, 1700432 (2017).
 45. Materlik, R., Kuneth, C. & Kersch, A. The origin of ferroelectricity in Hf_{1-x}Zr_xO₂: A computational investigation and a surface energy model. *J. Appl. Phys.* **117**, 134109 (2015).
 46. Batra, R., Huan, T. D., Jones, J. L., Rossetti, G. & Ramprasad, R. Factors Favoring Ferroelectricity in Hafnia: A First-Principles Computational Study. *J. Phys. Chem. C* **121**, 4139 (2017).
 47. Huan, T. D., Sharma, V., Rossetti, G. A. & Ramprasad, R. Pathways towards ferroelectricity in hafnia. *Phys. Rev. B - Condens. Matter Mater. Phys.* **90**, 064011 (2014).
 48. Mulder, M. Epitaxial hafnium zirconate on GaN by pulsed laser deposition. (University of Twente, 2019).

49. Wakiya, N., Yoshida, M.. *Grain boundary Engineering in Ceramics*. (American Ceramic Society, 2000).
50. Ishigaki, H., Yamada, T., Wakiya, N., Shinozaki, K. & Mizutani, N. Effect of the Thickness of SiO₂ under Layer on the Initial Stage of Epitaxial Growth Process of Ytria-Stabilized Zirconia (YSZ) Thin Film Deposited on Si(001) Substrate. *J. Ceram. Soc. Japan* **109**, 766 (2001).
51. Wang, S. J. & Ong, C. K. Epitaxial Y-stabilized ZrO₂ films on silicon: Dynamic growth process and interface structure. *Appl. Phys. Lett.* **80**, 2541 (2002).
52. Lubig, A., Buchal, C., Guggi, D., Jia, C. L. & Stritzker, B. Epitaxial growth of monoclinic and cubic ZrO₂ on Si(100) without prior removal of the native SiO₂. *Thin Solid Films* **217**, 125 (1992).
53. Bardal, A., Matthée, T., Wecker, J. & Samwer, K. Initial stages of epitaxial growth of Y-stabilized ZrO₂ thin films on a-SiO_x/Si(001) substrates. *J. Appl. Phys.* **75**, 2902–2910 (1994).
54. Dubbink, D., Koster, G. & Rijnders, G. Growth mechanism of epitaxial YSZ on Si by Pulsed Laser Deposition. *Sci. Rep.* **8**, 5774 (2018).
55. Hirai, T. *et al.* Crystal and Electrical Characterizations of Oriented Ytria-Stabilized Zirconia Buffer Layer for the Metal/Ferroelectric/Insulator/Semiconductor Field-Effect Transistor. *Jpn. J. Appl. Phys.* **35**, 4016–4020 (1996).
56. Fenner, D. B. *et al.* Reactions at the interfaces of thin films of Y-Ba-Cu- and Zr-oxides with Si substrates. *J. Appl. Phys.* **69**, 2176–2182 (1991).
57. Gsell, S., Fischer, M., Bauer, T., Schreck, M. & Stritzker, B. Ytria-stabilized zirconia films of different composition as buffer layers for the deposition of epitaxial diamond/Ir layers on Si(001). *Diam. Relat. Mater.* **15**, 479 (2006).
58. Ockenfuß, G. *et al.* Preparation and growth of YSZ buffer layers and YBa₂Cu₃O₇ - films on silicon (100). *Phys. C Supercond.* **180**, 30–33 (1991).
59. Myoren, H., Nishiyama, Y., Fukumoto, H., Nasu, H. & Osaka, Y. As-Grown Preparation of Superconducting Epitaxial Ba₂YCu₃O_x Thin Films Sputtered on Epitaxially Grown ZrO₂/Si(100). *Jpn. J. Appl. Phys.* **28**, 351–355 (1989).

60. Bunt, P., Varhue, W. J., Adams, E. & Mongeon, S. Initial Stages of Growth of Heteroepitaxial Yttria-Stabilized Zirconia Films on Silicon Substrates. *J. Electrochem. Soc.* **147**, 4541 (2000).
61. Ourmazd, A., Taylor, D. W., Rentschler, J. A. & Bevk, J. Si→SiO₂ transformation: Interfacial structure and mechanism. *Phys. Rev. Lett.* **59**, 213–216 (1987).
62. Ohdomari, I., Akatsu, H., Yamakoshi, Y. & Kishimoto, K. The structural models of the Si/SiO₂ interface. *J. Non. Cryst. Solids* **89**, 239–248 (1987).
63. Hane, M., Miyamoto, Y. & Oshiyama, A. Atomic and electronic structures of an interface between silicon and β-cristobalite. *Phys. Rev. B* **41**, 12637–12640 (1990).
64. Ohtaka, O. *et al.* Structural Analysis of Orthorhombic Hafnia by Neutron Powder Diffraction. *J. Am. Ceram. Soc.* **78**, 233–237 (1995).

Figure Captions

Figure 1. Texture and phase analysis on 10 nm (1-x)HfO₂: xZrO₂ films grown on Si (111)

(a) Representative pole figure obtained about $2\theta=30^\circ$ on film with $x=0.7$, consistent with $\langle 111 \rangle$ out of plane texture. The three non-out-of-plane $\{111\}$ poles, P1-P3, arising out of the film are centered at $\chi \approx 71^\circ$ and separated in ϕ by 120° . Rotated 180° from the film pattern, we see weak spots arising from the tail of substrate non-out-of-plane $\{111\}$ poles at $2\theta=28.44^\circ$. Pole figure symmetry looks similar for $x=0.5$ and $x=0.85$ (Supplementary Fig. 1). (b-d) Pole-slicing, or θ - 2θ scans around P1, P2 and P3 for $x=0.5$ (b), 0.7 (c) and 0.85 (d). While $x=0.5$ (b) shows just the monoclinic $\{111\}$ peaks, a low-volume phase peak starts evolving from $x=0.7$ (c) at $2\theta \approx 30.2^\circ$ and intensifies at $x=0.85$ (d).

Figure 2. Determination of symmetry for the low-volume phase on Si (111)

(a) Gaussian fits for the non-out-of-plane $\{111\}$ poles P1-P3 and the plane normal (out-of-plane) corresponding exclusively to the low-volume phase for films with $x=0.85$. The raw data (Fig. 1d), and 3 peak fitting procedure (two monoclinic, and one low-volume phase) is shown in Supplementary Fig. 1b. (b) Peak positions of the P1-P3 compared to the plane normal obtained from (a). This clearly reveals a 3:1 multiplicity, or an r-phase. Error estimation is shown in Supplementary Fig.2. r-phase is further corroborated from pole-slicing of the $\{001\}$

poles shown in Supplementary Fig. 3. (c) Cross-sectional HAADF-STEM image of TiN-HZO ($x=0.7$)-Si MIS capacitor (obtained along the $\langle 1-10 \rangle$ zone of the substrate), showing various $\{111\}$ d-spacings. $d_{\{11-1\}}=2.81\pm 0.02$ Å, and $d_{\{111\}}=3.11\pm 0.02$ Å are quite clearly bulk m-phase parameters. The low-volume phase becomes a suspect when $d_{\{111\}}$ values are measured between 2.90 and 3.00 Å. (d) Zoomed-in look at the Si-HZO interface, boxed in yellow in (c). The interface with Si on the left contains re-grown a-SiO_x (<1 nm). We clearly see an m-phase right above it. The region on the right has no a-SiO_x, but instead a direct connection between HZO and the crystalline substrate. That is a low-volume phase. (e) R3 phase HAADF-STEM multislice image simulation at lamella thickness of ~20 nm (defocus ~0). This quite corresponds to our image. In particular the contrast fluctuations along the red line ($\langle 112 \rangle$ direction) in (d) are shown in (f), do not appear in o or t-phase, and are quite unique to the r-phases (as can be seen visually in (e)).

Figure 3. Interface structure and epitaxy on Si (111)

(a) Bright field (BF) cross-sectional STEM image with inverted contrast of the interface. BF mode provides better contrast for lighter elements, and thus this mode of imaging is being reported. Clearly, we see 2-3 monolayers of interface with a different structure than both Si substrate and the HZO. This is a c-SiO₂ interface, with β -cristobalite or tridymite being the most likely phases. (b) Schematic of epitaxy on Si, with β -cristobalite at the interface. It provides the compressive strain necessary to stabilize the r-phase on HZO. (c) I-V, and corresponding P-V loops obtained from MIS capacitor structure of TiN-HZO ($x=0.7$)-Si at 1000 Hz, and 10 K. Although quite leaky on the inversion side (negative voltage), we nevertheless see switching peaks in the I-V curves. P_s is quite low, since the majority of the film is in a non-polar monoclinic phase. But this is a proof-of-concept that the r-phase is indeed polar.

Figure 4. Texture measurements on HZO ($x=0.7$) on Si(100) at different thicknesses

Pole figures obtained about $2\theta=31^\circ$ (corresponding to $d_{\{111\}}$) and about $2\theta=34^\circ$ (corresponding to $d_{\{100\}}$) on 5 nm (a,b), 10 nm (c,d) and 20 nm (e,f) HZO films grown on Si (100). (a,b) In 5 nm thick samples 4 $\{111\}$ poles separated in ϕ by 90° are observed at $\chi\approx 53^\circ$, and $\{001\}$ pole at $\chi\approx 0^\circ$ clearly showing that the films are textured with $\langle 001 \rangle$ oriented out of plane. (c,d) In 10 nm thick samples, apart from the poles observed for 5 nm, there are some extra satellite $\{111\}$ poles at $\chi\approx 58^\circ$ forming a triangular pattern, and 4 $\{001\}$ satellites centered around $\chi\approx 8^\circ$ (spread=8-10°) separated in ϕ by 90° . All these patterns can be mathematically explained through the coexistence of various monoclinic domains (each contributing to a different Bragg

reflection, see Supplementary information). (e,f) What were just satellite spots in 10 nm samples, become the main Bragg spots at 20 nm thickness.

Figure 5. Phase coexistence and domains

(a) From figure 4c (10 nm film thickness), one of the $\{111\}$ poles and its corresponding satellites are zoomed in. The black pixel corresponds to $\chi = 53^\circ$, where the $\{111\}$ main pole is the most intense. The grey pixels correspond to $\chi = 58^\circ$ where the satellites are the most intense. A progression from black to grey traverses through orange and red pixels, which correspond to purposeful misalignment (“well aligned” conditions are obtained by maximizing the intensity, which would ignore information from orange and red pixels). (b) With the color coding scheme as described in (a), pole slicing was then performed at various χ values from black pixel to the grey pixel (pixel positions numbered 1 to 11). At the black (1) or grey (10, 11) pixels, peaks corresponding to monoclinic $\{111\}$ d-spacings are observed. In the orange (2, 3) and red (4, 6) pixels however, a $\{111\}$ peak corresponding to a low-volume phase appears at $2\theta \approx 30.2^\circ$. (c) The various domains that correspond to the pole-figures presented in Figure 4. The left one shows a monoclinic domain with a-b plane of HZO// Si(100). This is very well oriented growth observed at low film thicknesses (5 nm). The center panel shows a monoclinic domain with a-b plane misaligned from the Si (100) surface. Negative and positive misorientations can give rise to an accordion-like zig-zag pattern. The right most panel shows the domain from the low-volume phase (which can be shown to be orthorhombic from TEM results to follow)

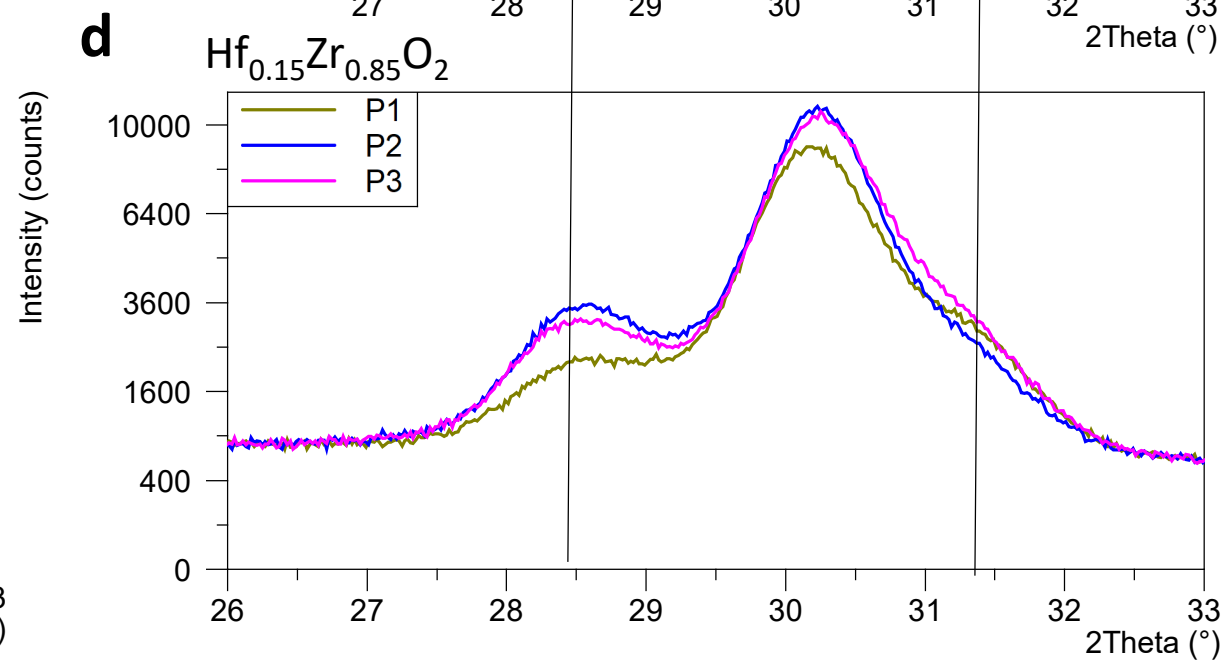
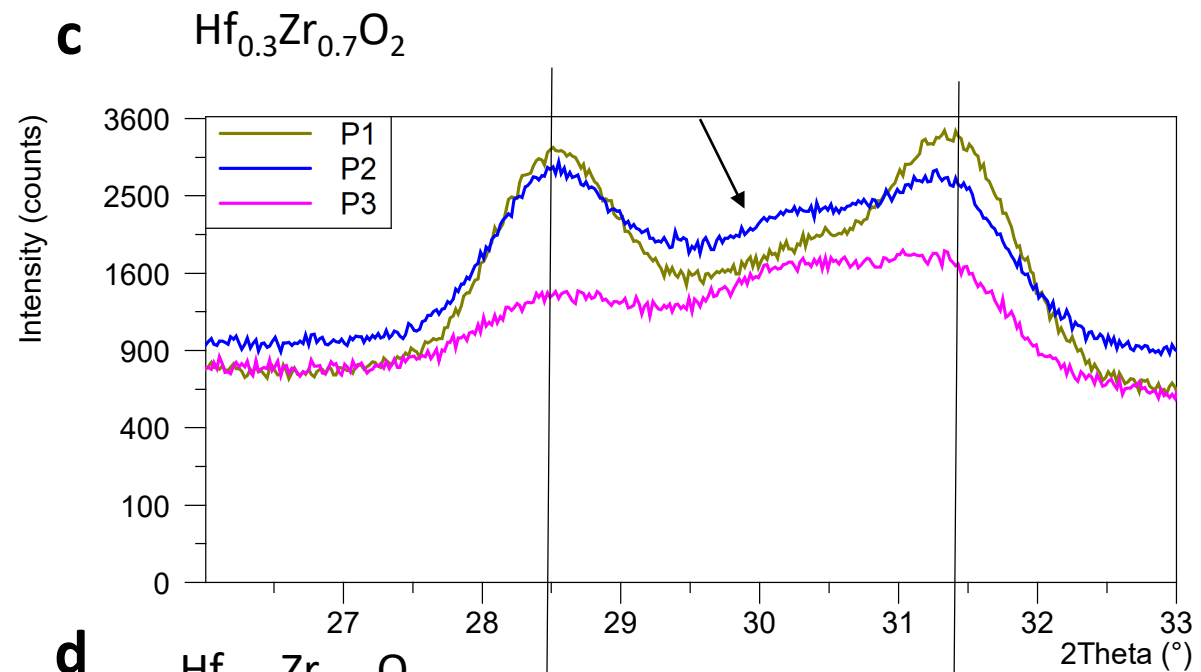
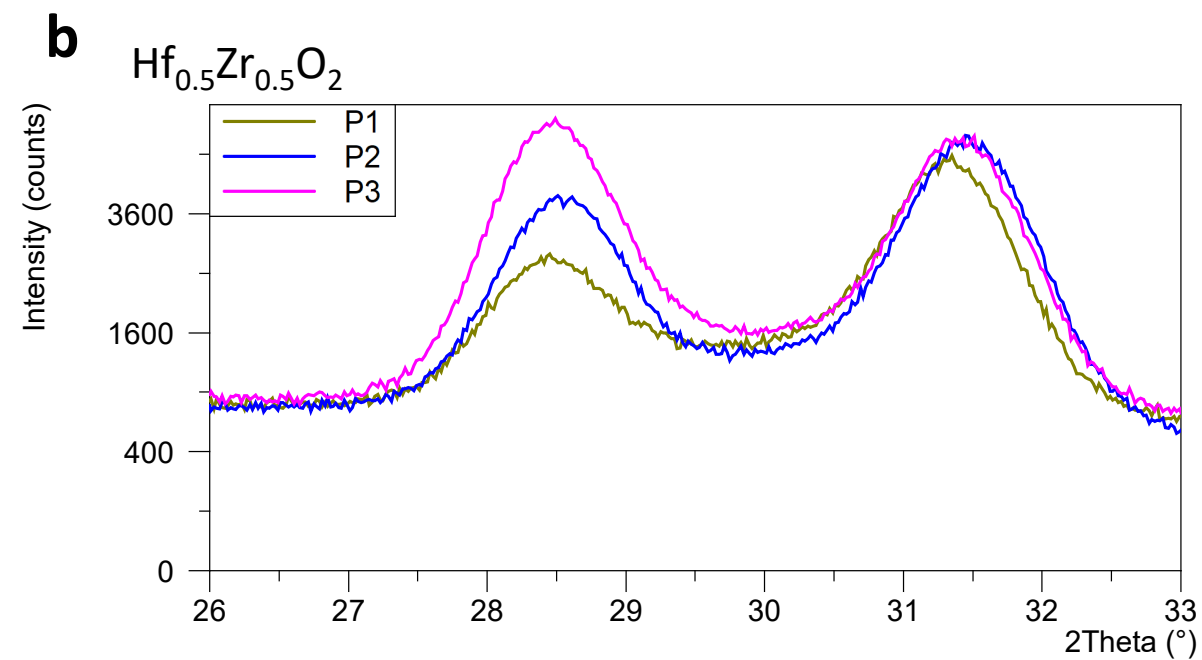
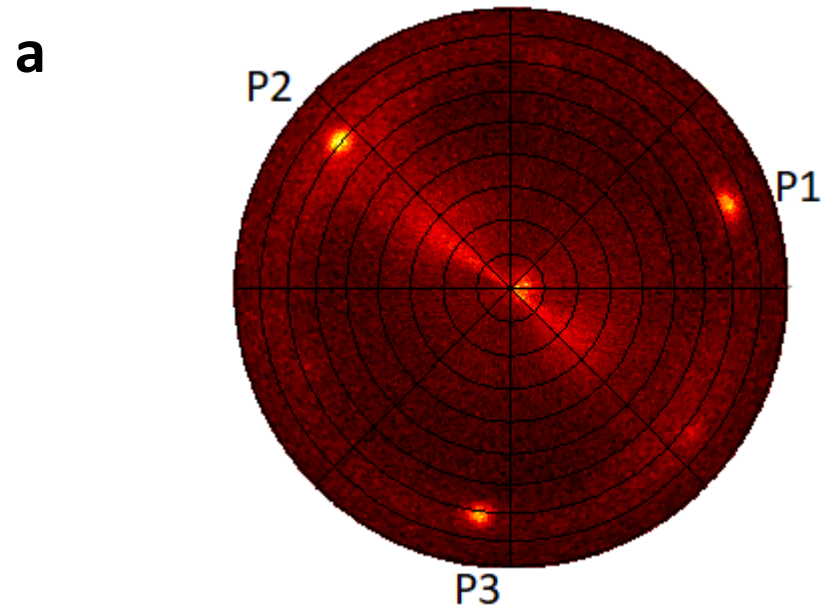
Figure 6. Monoclinic domains, orthorhombic domains, and accordions of HZO on Si (100)

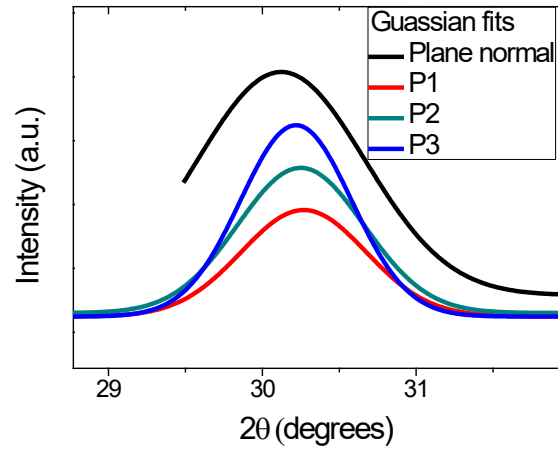
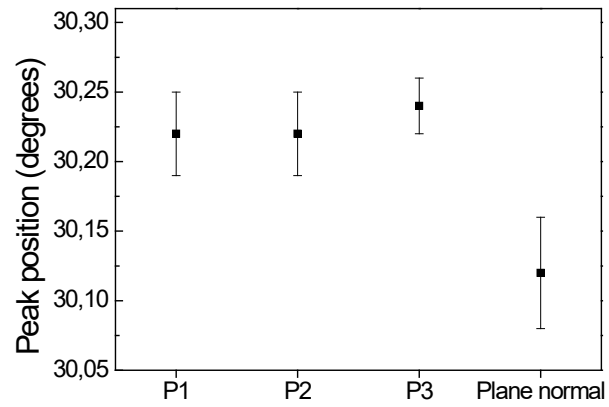
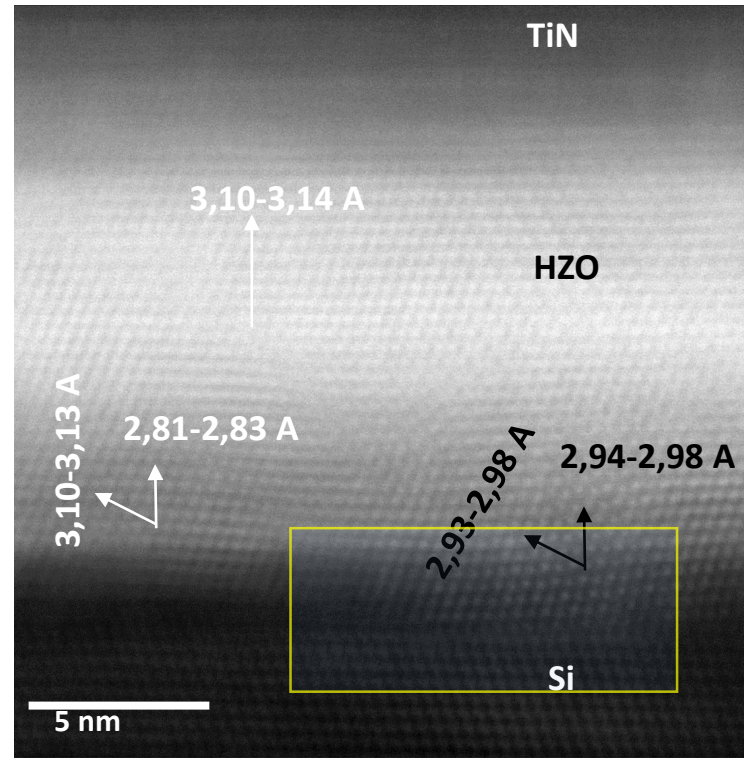
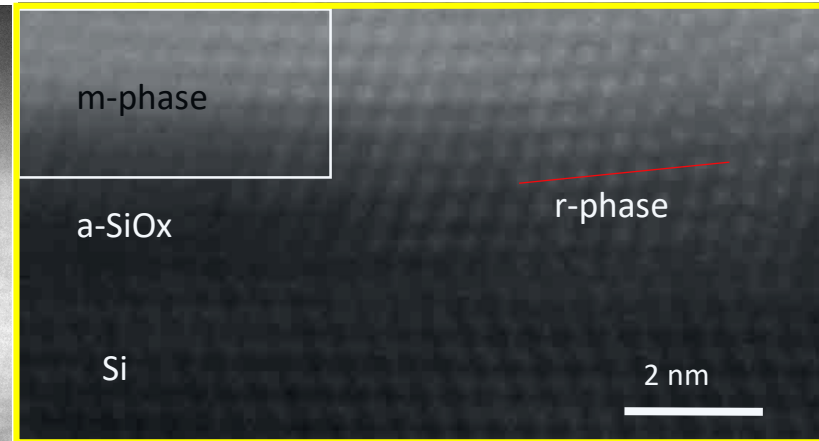
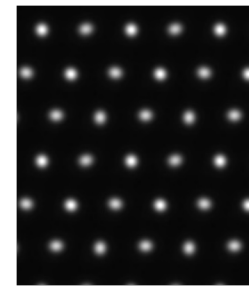
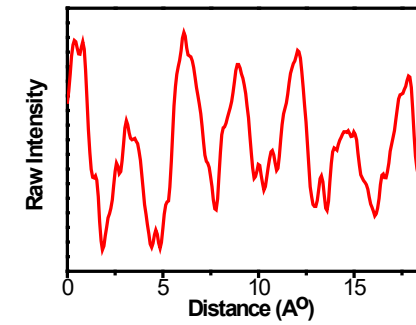
(a) Overview cross-sectional HAADF-STEM image along the [010] zone axis, of 10 nm thick HZO ($x=0.7$), showing a clear accordion-like morphology. (b) Zoomed-in view of the region surrounded by blue box in (a), showing intersection of two domains. D-spacings estimated from the Fast Fourier transform (FFT) obtained from the domain on the left confirm a monoclinic phase. Furthermore, the monoclinic angle (β) can be directly read from the FFT to be $\sim 81^\circ$ in this image. The ab plane is misoriented with respect to the substrate (normal) by 9° . HAADF-STEM multislice image simulations of monoclinic phase, clearly match our domain. If the domain on the left is positively misoriented with the substrate, the domain on the right is negatively misoriented, and their intersection gives rise to an accordion pattern. (c) Zoomed-in view of the region surrounded by the red box in (a). The d-spacing obtained from FFT clearly shows that this is in the o-phase ($d_{(002)} = 2.51 \pm 0.02 \text{ \AA}$, and $d_{(200)} = 2.57 \pm 0.02 \text{ \AA}$). HAADF-STEM image simulations match the real image (with zig-zag arrangement of atomic columns along

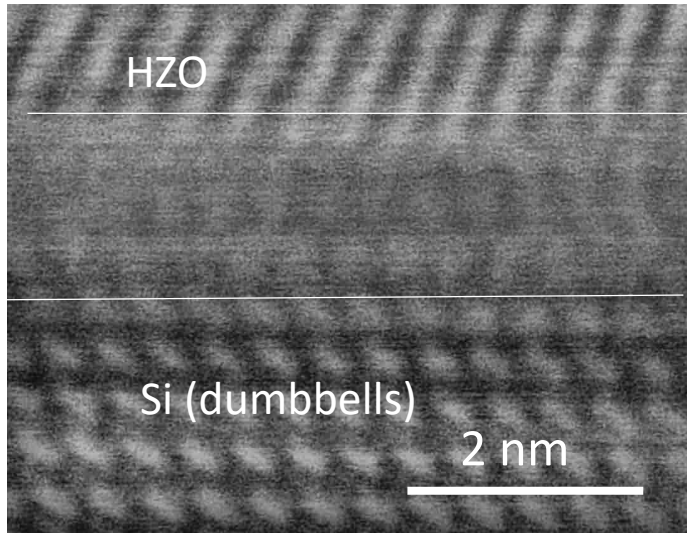
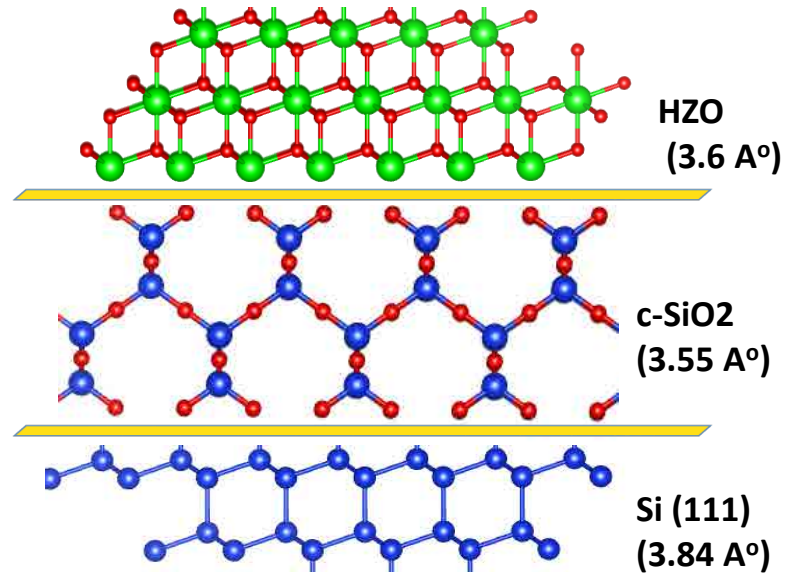
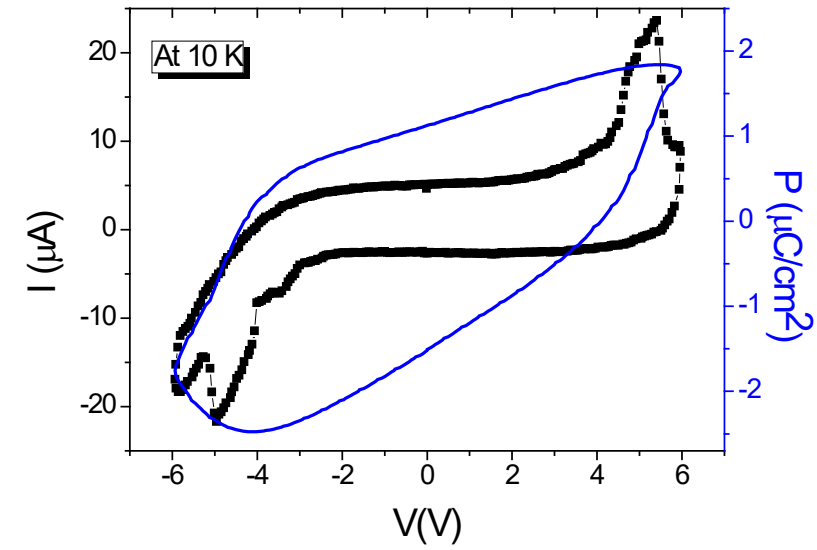
[001]). Simulations from different phases are compared in supplementary Fig. 5. The polar axis however, is the c-axis which is in-plane.

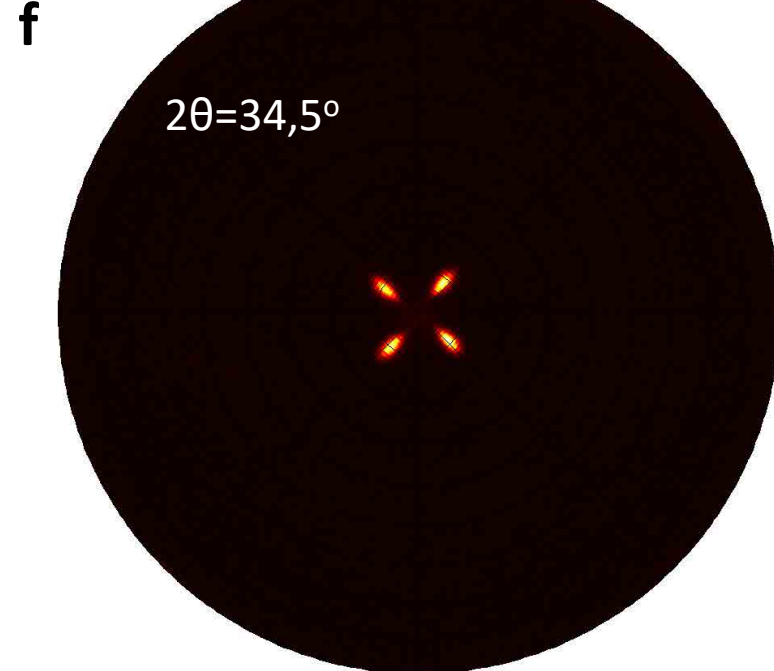
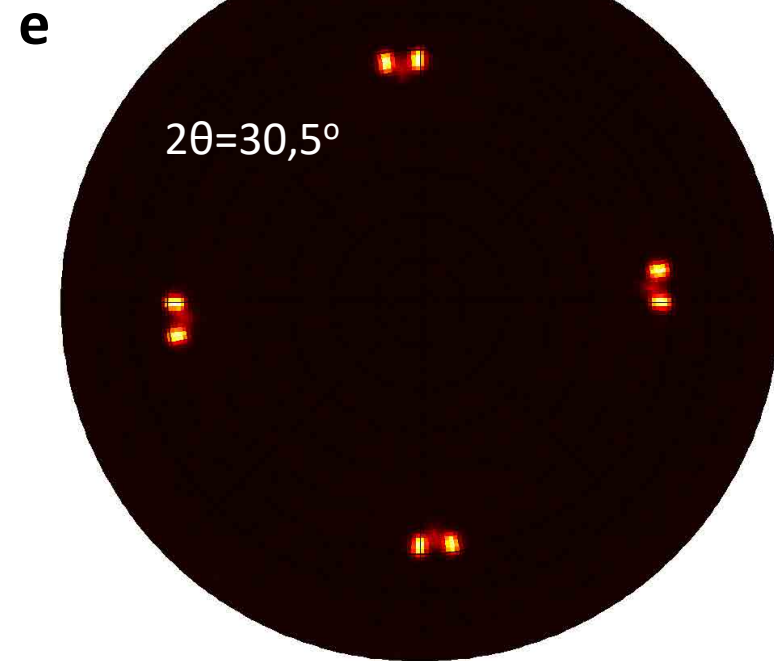
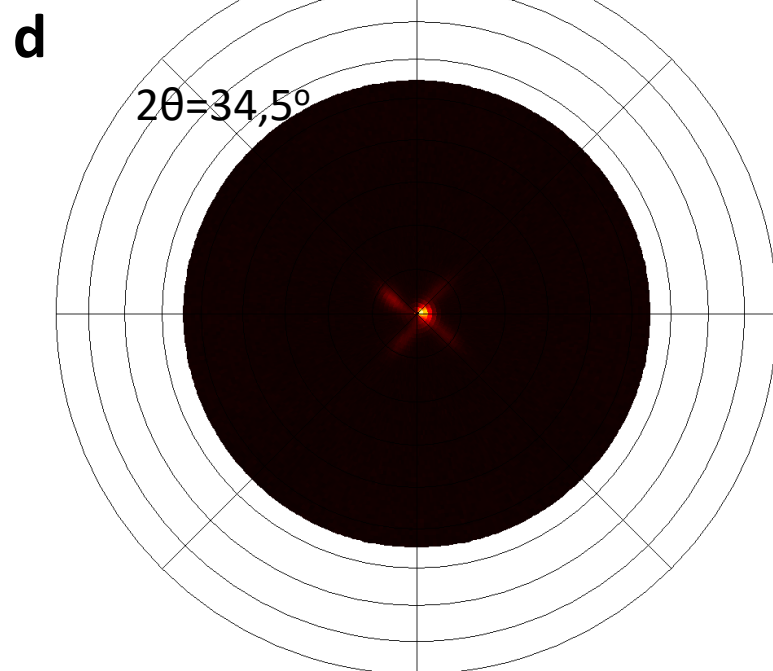
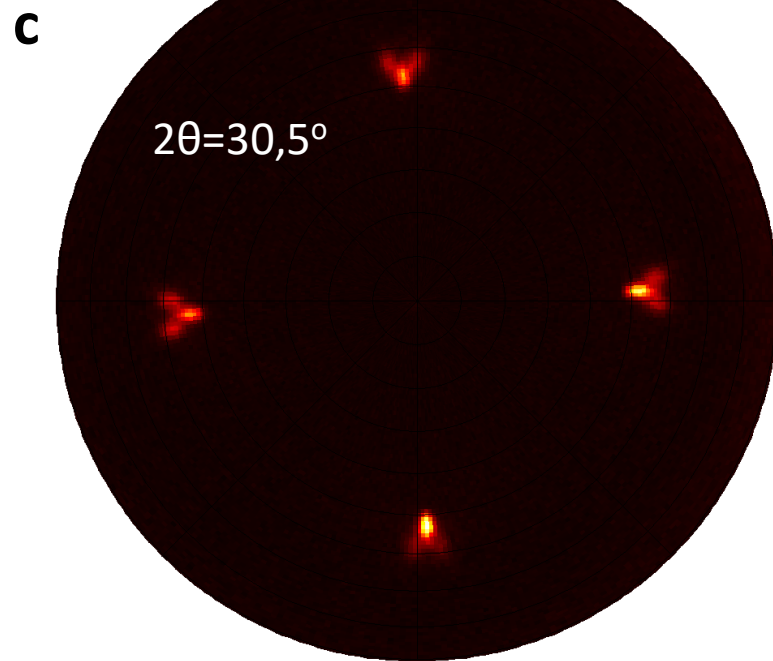
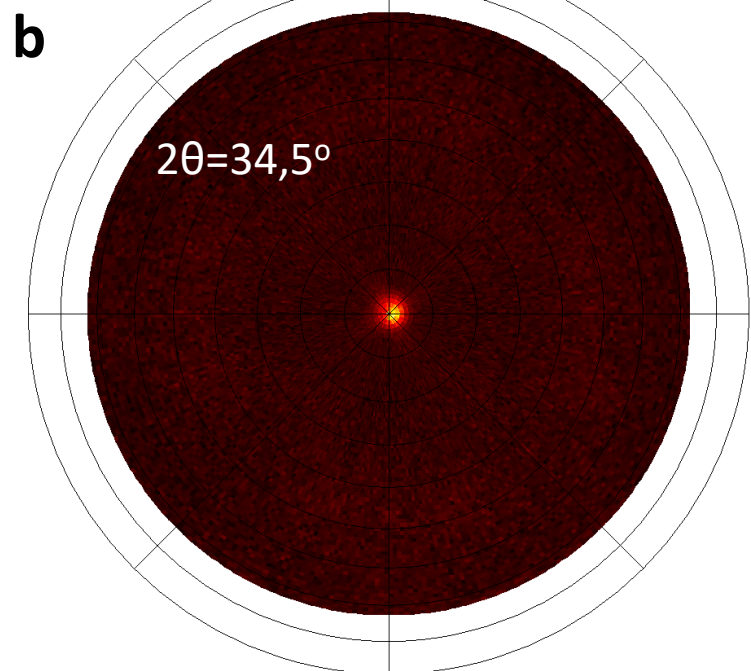
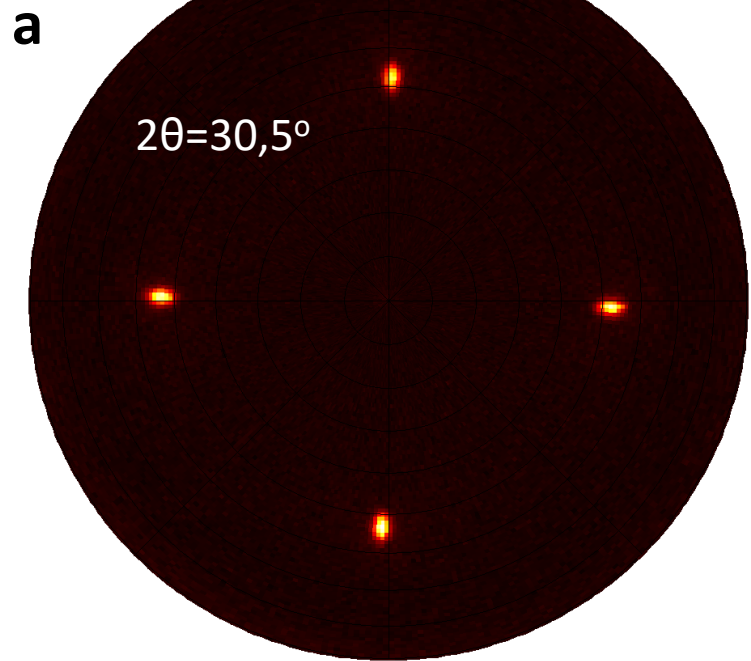
Figure 7. Interface and epitaxy on Si (100)

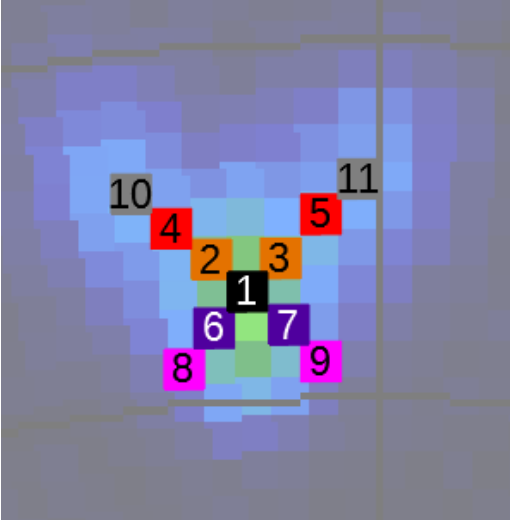
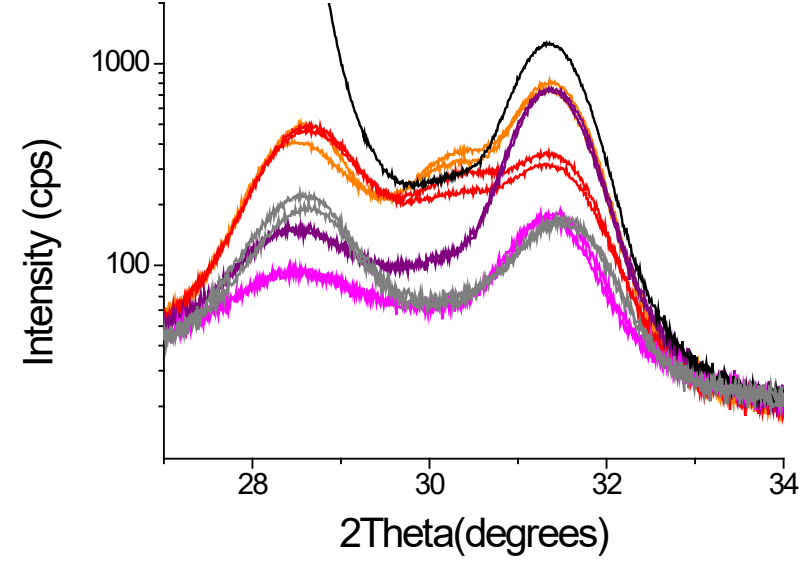
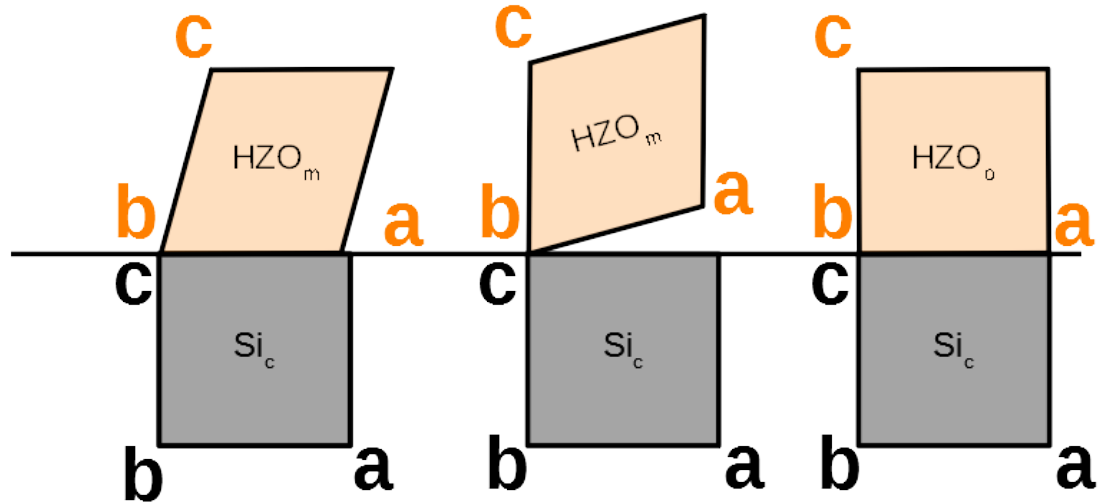
(a,b) EDS chemical maps, and Wiener-filtered HAADF-STEM image clearly showing a re-grown a-SiO_x layer of ~ 1 nm between Si (100) and HZO (x=0.7). (c) Zoomed-in view of Wiener filtered image in (b). There is also an interfacial crystalline structure (boxed in blue) at the interface of Si and a-SiO_x, most likely belonging to c-SiO₂ in β-cristobalite phase. This enables orientational relationship with HZO layer.

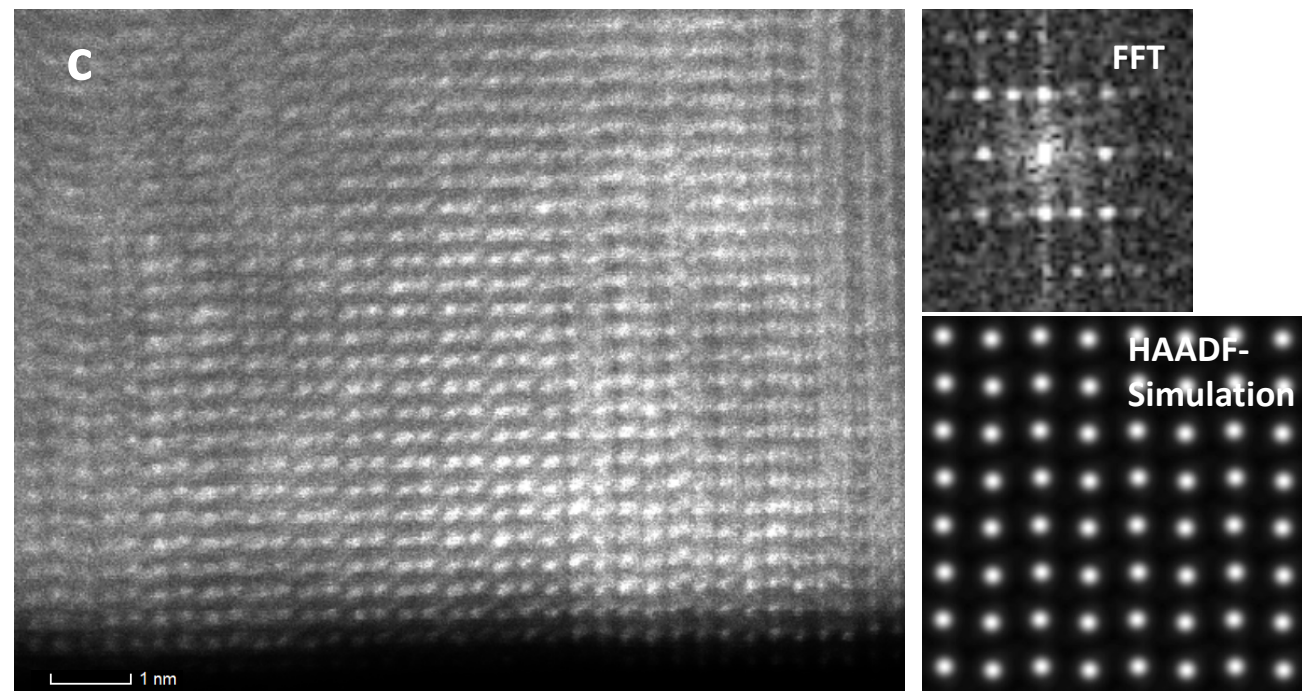
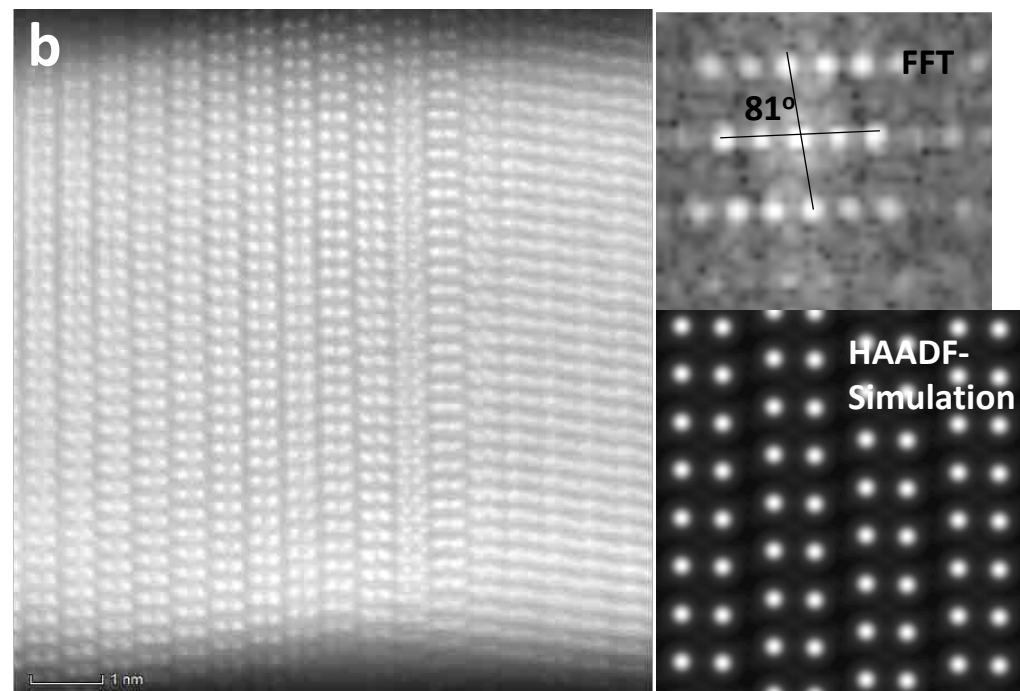
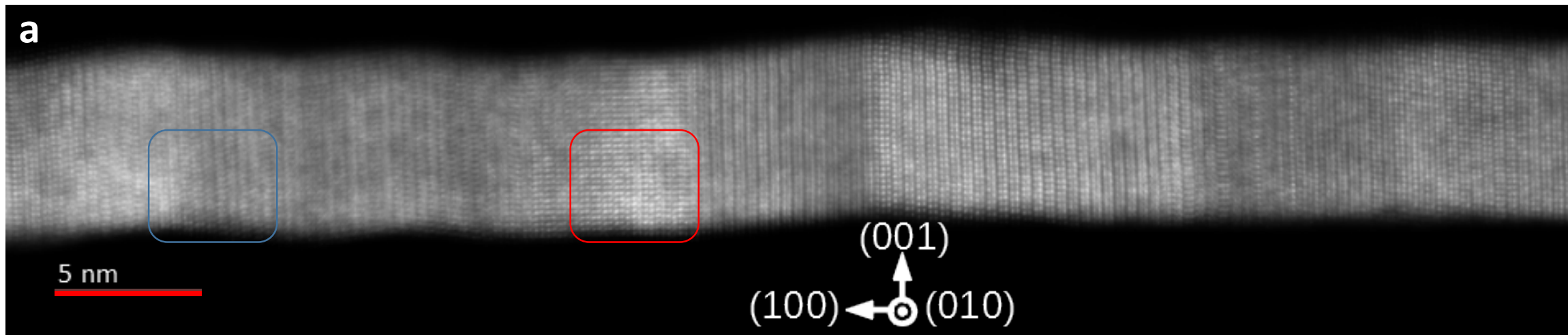


a**b****c****d****e****f**

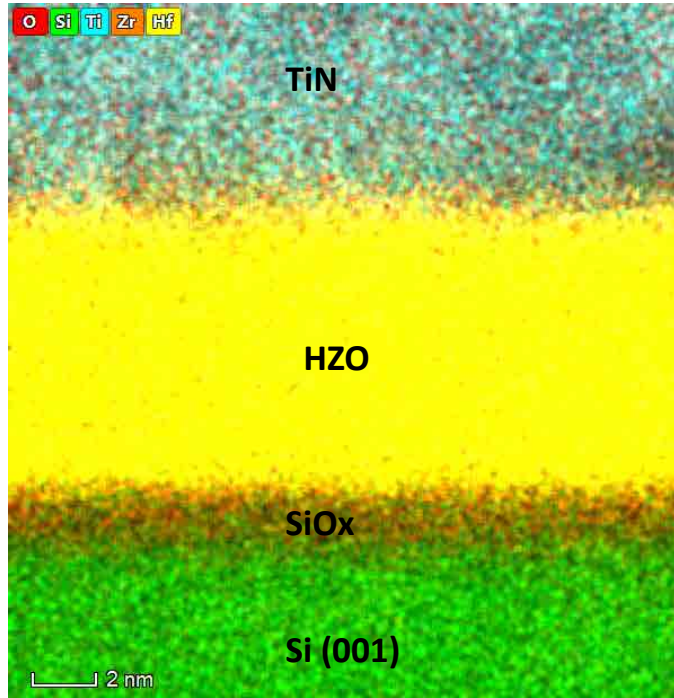
a**b****c**



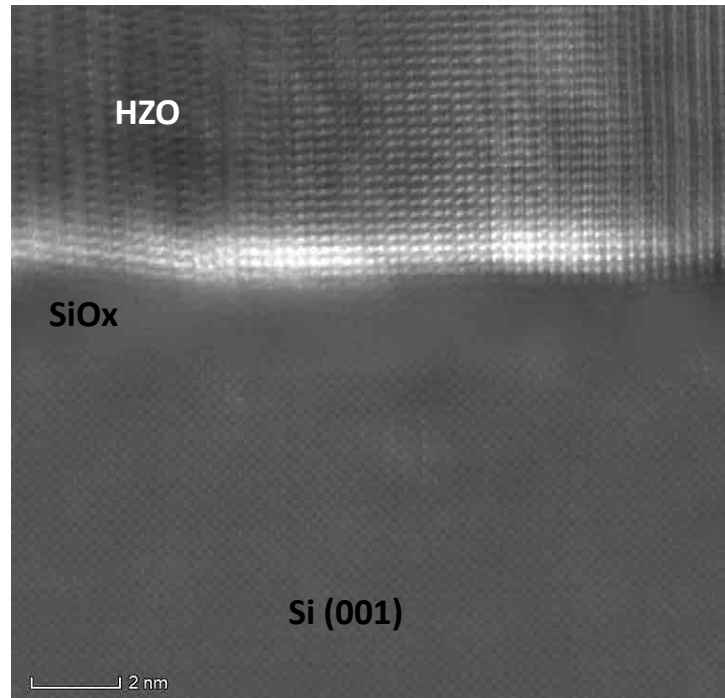
a**b****c**



a



b



c

